CFD Letters

Journal homepage:
https://semarakilmu.com.my/journals/index.php/CFD_Letters/index
ISSN: 2180-1363

Evaluation of the Interconnection of a Biomethane Microturbine in an Absorption Refrigeration System

Juan Sebastián Fernández Herazo[1*], Rafael Antonio Ramírez Restrepo[1], Andrés Rodríguez Toscano[2], Catalina Vallecía Burgos[1]

[1] Department of Mechanical Engineering, Faculty of Engineering, Universidad del Atlántico, Barranquilla, Colombia
[2] Energy Department, Faculty of Engineering, Universidad de la Costa, Barranquilla, Colombia

ARTICLE INFO

Article history:
Received 2 January 2024
Received in revised form 7 February 2024
Accepted 8 March 2024
Available online 31 October 2024

Keywords:
Biomethane microturbine; absorption refrigeration system; CFD analysis; energy generation; environmental impact; exergy balances; LiBr-H_2O system

ABSTRACT

This article evaluates the performance and environmental impact of a combined system of natural gas microturbine and absorption refrigeration system. The objective of the study is to evaluate the interconnection of a biomethane microturbine in an absorption refrigeration system. The study applies energy and exergy balances to each component of the system, using EES software for the simulation. The microturbine is a Capstone C600s model with a nominal power of 600 kW, and the absorption chiller is a single-stage LiBr-H_2O system with a cooling capacity of 680.7 kW. The results show that the microturbine achieves a thermal efficiency of 34%, an exergetic efficiency of 86%, and a net power output of 585.4 kW. At the same time the absorption chiller has a coefficient of performance (COP) of 0.7 and 680.7 kW with generator water temperature inlet of 100 °C. On the other hand, this study identifies the most efficient points of interconnection between the two systems. The combined system reduces the CO_2 equivalent emissions by 700 to 900 tons/year compared to conventional systems. The behaviour of the interconnection heat exchanger is also evaluated using Computed Fluid Dynamics. The investigation concludes that the interconnection of a natural gas microturbine and an absorption refrigeration system is a promising alternative that can optimize both technical and economic aspects of energy generation and utilization, while mitigating environmental problems.

1. Introduction

The rising need for energy, alongside escalating environmental worries, has driven the quest for better, more sustainable methods in energy production and usage. The Paris Climate Agreement (the Agreement), adopted by the Parties to the United Nations Framework Convention on Climate Change (UNFCCC) in 2015, has been signed by 197 countries and went into force in November of 2016. It is arguably the first truly global climate change agreement and aims to put the world on track to eventually stabilize greenhouse gas (GHG) emissions at a level that would avoid dangerous climate change according to Liu *et al.,* [1]. This push has prompted industrial firms to adopt innovative

* *Corresponding author.*
E-mail address: jsfernandez@mail.uniatlantico.edu.co (Juan Sebastián Fernández Herazo)

https://doi.org/10.37934/cfdl.17.3.124147

management systems, aiming to tackle the urgent call for cleaner and more efficient energy practices. For instance, integrating coconut shell biomass as an alternative and supplementary thermal source offers a promising solution to the intermittent nature of solar-powered systems, as explored by Meriño *et al.,* [2]. With the escalating use of fossil fuel-derived energies, there is a growing imperative to shift towards renewable energy sources as an alternative to replace conventional coal-based electricity generation methods. This transition is essential to address environmental concerns and promote sustainable energy practices reviewed by Niu *et al.,* [3]. This transition is also mirrored in the historical development of turbine technology, with gas turbines tracing their roots back to the mid-20th century through the development of aircraft engines. Similarly, microturbines have evolved from auxiliary turbines installed in aircraft for the provision of electricity and heat. Attempts were made to employ similar devices as power units in automobiles in the 1970s, but the technology did not meet with success investigated by Breeze *et al.,* [4] because gas turbine engines operate most efficiently at constant output speed (i.e., constant rpm), they have not performed well as power units in automobiles and other devices requiring variable-speed shaft output.

Transitioning from fossil fuels to natural gas or renewables is crucial for reducing carbon emissions and ensuring energy security amidst evolving needs and environmental challenges. Innovations like supercritical CO2 Brayton cycles and natural gas microturbines show promise in meeting energy demands while mitigating environmental impacts. Boukhanouf *et al.,* [5] delve into the advantages and characteristics of natural gas microturbines, highlighting their potential contributions to various applications in the field of energy generation and emphasizing their ability to effectively regulate emissions. Meanwhile, Gautam *et al.,* [6] explore the additional benefits of natural gas microturbines, emphasizing their potential for parallel modular configurations to enhance energy reliability and their cost-effectiveness in terms of maintenance.

In the domain of air conditioning technology, conventional refrigerants used in vapor compression refrigeration systems, such as CFCs and HCFCs, have detrimental effects on the environment, including contributions to global warming and ozone layer degradation. Kasaeian *et al.,* [7] reviews the experimental and theoretical studies that have been carried out with environmentally friendly refrigerants such as hydrocarbons, hydrofluorocarbons, R744 (carbon dioxide), hydrofluoro olefin, and nanorefrigerants. In addressing this concern, environmentally friendly refrigeration systems have been developed, including absorption, desiccant, and adsorption chillers. These systems offer the added advantage of being able to operate with various low-grade energy sources, such as residual energy from industrial processes and solar power. Absorption chillers are categorized based on the number of stages: single-stage, two-stage, and three-stage.

Hwang *et al.,* [8] has presented and analyzed the efficiency potential of a refrigeration system that integrates a microturbine with an absorption chiller. The system is comprised of a low-temperature compression system and a high-temperature absorption system. Seyfouri *et al.,* [9] explore the synergies between these components and assesses the overall efficiency of the combined system, providing insights into its potential for enhanced performance in cooling applications. Kaikko *et al.,* [10] analyze the technical and economic performance of a microturbine in combined heat and power (CHP) generation based in a simulation model to assess various operational scenarios and environmental conditions. The results demonstrate that the microturbine can reduce fuel consumption and CO_2 emissions, and that the levelized cost of energy depends on the electricity tariff and natural gas prices. Microturbines commonly utilize natural gas as their energy source studied by Hwang *et al.,* [8]. Understanding that generating energy from alternative sources will contribute to mitigating climate change and minimizing risks to the environment, to provide a clean and sustainable environment to our modern society, the prospects of biogas and biomethane, as well as

their generation methods, have increased exponentially, always with the aim of sustainable energy development in support of the green transition. According to Argalis *et al.,* [11] Biogas produced from waste contains about 40–70% CH_4 and needs to be upgraded to a CH_4 content of >95% to be called biomethane. Biomethane is a renewable fuel that can completely replace fossil natural gas because of the similarities in its composition. By using renewable energy, greenhouse gas emissions can be reduced.

The interconnection of a natural gas microturbine in an absorption refrigeration system is presented as an innovative and promising alternative that combines electric power generation with cooling, optimizing both technical and economic aspects. Desideri *et al.,* [12] explore the synergies achieved through the integration, emphasizing the potential benefits in terms of efficiency and cost-effectiveness in dual-generation systems. The decision to employ a gas microturbine as the main engine in a microgrid represents an intelligent solution that allows for quick response times and the integration of renewable and cutting-edge technologies. Konečná *et al.,* [13]. study the advantages of choosing a gas microturbine in the context of microgrid systems, highlighting its role in facilitating flexibility, efficiency, and the seamless incorporation of emerging energy solutions. This study focuses on the technical and environmental evaluation of the solution involving the interconnection of a gas microturbine C600s and a previously analyzed and studied 680.7 kW absorption chiller.

This document aims to examine the potential of implementing biomethane, evaluating the different substrate options that lead to profitable performance in order to provide a basis for future research. The article delves into the assessment of the combined system, examining its performance and environmental impact, providing a comprehensive understanding of the integrated microturbine and absorption chiller configuration by Seo *et al.,* [14], aims to analyze the viability, efficiency, and potential impact of the integrated system as a means of mitigating environmental problems. The objective is to contribute to knowledge in the field of energy and refrigeration, promoting the adoption of more sustainable systems in an ever-evolving world. Finally, it discusses the implications of the integrated system and offers ideas on its feasibility and effectiveness in meeting environmental challenges.

2. Methodology

This section presents a general description of the 600 kW natural gas microturbine (comprising three (3) modules of 200 kW each) and its operation. In this study, a Capstone C600s [15] microturbine is considered. The microturbine is a stationary power generation system that provides electrical energy for primary or backup applications, as well as for base load and/or capacity expansions. The system comprises a turbine engine, a solid-state power electronic system, a fuel system, and an outdoor enclosure. The key components of the turbine engine include a compressor, a recuperator (heat exchanger for exhaust gases), a combustion chamber, a turbine, and a generator. The turbine engine is air-cooled and supported by air-lubricated foil bearings (air bearings). The compressor impeller, turbine rotor, and generator rotor are mounted on a single shaft. A typical microturbine will utilize radial compressors and turbines instead of the axial components common in larger gas turbines. The compressor is likely to be single-stage, as is the turbine, both mounted on the same shaft with a combustion chamber between them. A high-speed generator will share the shaft, resulting in a compact design. Air bearings are often used to minimize friction, although conventional oil-lubricated bearings are also common. These small turbines have extremely high rotational speeds, typically between 40,000 and 120,000 revolutions per minute, and the generator output frequency is equally high, perhaps up to 1,000 Hz. Therefore, to adapt them to the grid frequency, these systems are equipped with power electronic frequency conversion hardware. This

has the advantage of conditioning the supply and controlling both voltage and frequency, and the unit should be able to operate independently of the grid if necessary. A typical microturbine employs a single-stage radial compressor with a relatively low compression ratio compared to the multistage compressors found in larger gas turbines, with typical compression ratios ranging from 3:1 to 4:1. To enhance efficiency, these machines often incorporate a recuperator, which captures energy from the turbine exhaust gases and uses it to preheat the compressed air before it enters the combustion chamber, with typical efficiency ranging from 25% to 30%. However, there are also microturbines that do not utilize a recuperator, which are more robust but less efficient, with an efficiency of around 15%. All components of the microturbine are typically integrated into a single package that simplifies connection to the electrical supply, making installation straightforward, which is one of the main attractions of this type of device as described by Breeze *et al.,* [4].

2.1 Energy Balance

Each component of the system (Figure 1) is treated as a control volume. Mass and energy balances are applied to each component according to Eq. (1) and Eq. (3), respectively. This approach ensures a comprehensive analysis of the system's behavior and performance.,

$$\sum \dot{m}_{in} - \sum \dot{m}_{out} = 0 \tag{1}$$

When applying the Reynolds Transport Equation to the first law of thermodynamics, Eq. (2) is obtained:

$$\frac{\partial}{\partial t}\int_{cv} e\rho d\forall + \int_{cs}\left(\breve{u} + \frac{p}{\rho} + \frac{v^2}{2} + gz\right)\rho \mathbf{V}\cdot\hat{\mathbf{n}}dA = \dot{Q}_{net,in} + \dot{W}_{net,in} \tag{2}$$

By discretizing Eq. (2), we obtain the energy balance, Eq. (3):

$$\sum \dot{m}_{in}h_{in} - \sum \dot{m}_{out}h_{out} + \sum \dot{Q} + \sum \dot{W} = 0 \tag{3}$$

Eq. (3) represents the energy balance equation, where $\dot{m}$ is the mass flow rate, h is the specific enthalpy of the fluid, and $\dot{Q}$ and $\dot{W}$ are the heat and power flow, respectively. It is assumed that each component of the combined cycle operates in a steady state.

In the specific case of the absorption circuit, the subsequent section provides:

$$\dot{Q}_e + \dot{Q}_g - \dot{Q}_c + \dot{W}_p = 0 \tag{4}$$

In this equation, $\dot{Q}_e$, $\dot{Q}_g$, $\dot{Q}_c$ denote the heat flows through the evaporator, generator, and compressor, respectively, while $\dot{W}_P$ corresponds to the power of the LiBr-Water solution pump. The circulation factor, f is defined as the ratio of the lean solution flow rate to the coolant flow rate. Mathematically it can be written as:

$$f = \frac{\dot{m}_w}{\dot{m}_r} \tag{5}$$

Where $\dot{m}_w$ and $\dot{m}_r$ are the mass flows of the LiBr-Water weak solution and refrigerant, respectively.

2.2 Exergetic Balance

The specific exergy calculation is carried out by neglecting the variation of kinetic and potential energy, according to Eq. (6):

$$ex = h - h_0 - T_0(s - s_0) \tag{6}$$

Where h_0 and s_0 are the enthalpy and entropy of the reference state, respectively, calculated under steady-state conditions of T_0 = 25 °C and P_0 = 101,325 kPa. For the study, it is assumed that the exhaust gas is standard air.

The exergy balance for steady-state control volumes is applied to each component of the system according to Eq. (7):

$$\sum \dot{m}_{in} ex_{in} - \sum \dot{m}_{out} ex_{out} + \dot{Q}\left(1 - \frac{T_0}{T}\right) - \dot{W} - \dot{E}x_D = 0 \tag{7}$$

Where $\dot{m}_{in} ex_{in}$ is the exergy flow entering the control volume, $\dot{m}_{out} ex_{out}$ is the exergy flow leaving the control volume, and $\dot{E}x_D$ is the rate of exergy destruction.

2.3 Computational Fluid Dynamics Analysis for Interconnection

In addressing the intricacies of turbulence interactions within a fluid system, the establishment of a set of equations becomes imperative to holistically solve its kinematic and dynamic characteristics according to Molina *et al.,* [16]. The pivotal tool for this endeavor is the Reynolds Transport Theorem, serving as a mechanism that transforms a general system analysis into a control volume analysis, contingent upon the nature of the control volume—whether fixed, deformable, or in motion. This discussion delves into the scenario of a deformable control volume undergoing arbitrary motion, forming the foundation for deriving the Navier-Stokes equations. The process commences with the application of Reynolds' transport theorem equation, specifically addressing volume and mass flow rate. This formulation defines a cubic differential element, solving it in adherence to the conservation of mass principle and resulting in the derivation of the continuity equation, succinctly expressed in Eq. (8):

$$\frac{\partial \rho}{\partial t} + \nabla \cdot (\rho \mathbf{V}) = 0 \tag{8}$$

By applying the concept of moment flow to a cubic differential element, it is imperative to account for all forces within the system, including body forces and surface forces. In this scenario, the sole external force is gravitational, while surface forces arise from stresses on all sides of the control surface, combining hydrostatic pressure and viscous stresses. This approach yields the linear momentum equation in its most simplified form:

$$\rho\mathbf{g} - \nabla p + \nabla \cdot \tau_{ij} = \rho \frac{d\mathbf{V}}{dt} \tag{9}$$

In the analysis of high-speed compressible flows and those featuring shock waves, the subsequent energy equation is employed for calculations:

$$\frac{\partial(\rho u_i)}{\partial t} + \frac{\partial}{\partial x_j}(\rho u_i u_j) + \frac{\partial P}{\partial x_i} = \frac{\partial}{\partial x_j}(\tau_{ij} + \tau_{ij}^R) + S_i \tag{10}$$

$$\frac{\partial \rho H}{\partial t} + \frac{\partial \rho u_i H}{\partial x_i} = \frac{\partial}{\partial x_i}\left(u_j(\tau_{ij} + \tau_{ij}{}^R) + q_i\right) + \frac{\partial p}{\partial t} - \tau_{ij}^R \frac{\partial u_i}{\partial x_j} + \rho\varepsilon + S_i u_i + Q_H \tag{11}$$

For calculation of high-speed compressible flows and flows with shock waves the following energy equation, Eq. (12) is used:

$$\frac{\partial \rho E}{\partial t} + \frac{\partial \rho u_i \left(E + \frac{p}{\rho}\right)}{\partial x_i} = \frac{\partial}{\partial x_i}\left(u_j(\tau_{ij} + \tau_{ij}^R) + q_i\right) - \tau_{ij}^R \frac{\partial u_i}{\partial x_j} + \rho\varepsilon + S_i u_i + Q_H \tag{12}$$

The fluid dynamics study involves fundamental equations, enhanced by fluid state equations defining characteristics. Empirical correlations enrich these equations with fluid properties like density, viscosity, and thermal conductivity in relation to temperature. The scope extends to inelastic non-Newtonian fluids. A non-Newtonian fluid can be characterized by a viscosity that varies with motion. Most non-Newtonian fluids have a molecular chain structure. In some of these fluids, the molecules tend to orient in planes of maximum tension resulting in a decrease in viscosity with an increasing velocity gradient; these fluids are called pseudo-plastics or 'shear-thinning' fluids. With increasing shear rate, the fluid is 'thinning'. In others, the viscosity will increase with an increasing velocity gradient according to Van Canneyt *et al.,* [17]. The analysis of the interconnection between the microturbine and the absorption chiller will be done using the SOLIDWORKS Flow Simulation tool which accommodates laminar and turbulent flows based on Reynolds numbers. The Favre-averaged Navier-Stokes equations predict turbulent flows, incorporating Reynolds stresses. SOLIDWORKS Flow Simulation uses transport equations and the k-ε model for closure. The modified k-ε turbulence model, with damping functions by Lam and, comprehensively describes laminar, turbulent, and transitional flows in homogeneous fluids. Adhering to turbulence conservation laws, this model offers a nuanced understanding of fluid dynamics across diverse flow regimes.

$$\frac{\partial \rho k}{\partial t} + \frac{\partial \rho k u_i}{\partial x_i} = \frac{\partial}{\partial x_i}\left(\left(\mu + \frac{\mu_t}{\sigma_k}\right)\frac{\partial k}{\partial x_i}\right) + \tau_{ij}^R \frac{\partial u_i}{\partial x_j} - \rho\varepsilon + \mu_t P_B \tag{13}$$

$$\frac{\partial \rho \varepsilon}{\partial t} + \frac{\partial \rho \varepsilon u_i}{\partial x_i} = \frac{\partial}{\partial x_i}\left(\left(\mu + \frac{\mu_t}{\sigma_\varepsilon}\right)\frac{\partial \varepsilon}{\partial x_i}\right) + C_{\varepsilon 1}\frac{\varepsilon}{k}\left(f_1 \tau_{ij}^R \frac{\partial u_i}{\partial x_j} + C_B \mu_t P_B\right) - f_2 C_{\varepsilon 2}\frac{\rho\varepsilon^2}{k} \tag{14}$$

$$\tau_{ij} = \mu s_{ij}, \tau_{ij}^R = \mu_t s_{ij} - \frac{2}{3}\rho k \delta_{ij}, s_{ij} = \frac{\partial u_i}{\partial x_j} + \frac{\partial u_j}{\partial x_i} - \frac{2}{3}\delta_{ij}\frac{\partial u_k}{\partial x_k}, P_B = -\frac{g_i}{\sigma_B}\frac{1}{\rho}\frac{\partial \rho}{\partial x_i} \tag{15}$$

Where $C_\mu = 0,09, C_{\varepsilon 1} = 1,44, C_{\varepsilon 2} = 1,92, \sigma_k = 1, \sigma_\varepsilon = 1,3, \sigma_B = 0,9, C_B = 1 if\ P_B > 0, C_B = 0 if\ P_B < 0$, the turbulent viscosity is determined from:

$$\mu_t = f_\mu \cdot \frac{C_\mu \rho k^2}{\varepsilon} \tag{16}$$

Lam and Bremhorst's damping function f_μ is determined from:

$$f_\mu = \left(1 - e^{-0,025 R_y}\right)^2 \cdot \left(1 + \frac{20,5}{R_t}\right), R_y = \frac{\rho \sqrt{k} y}{\mu}, R_t = \frac{\rho k^2}{\mu \varepsilon} \tag{17}$$

y is the distance from point to the wall and Lam and Bremhorst's damping function f_1 and f_2 are determined from:

$$f_1 = 1 + \left(\frac{0,05}{f_\mu}\right)^3,\ f_2 = 1 - e^{R_t^2} \tag{18}$$

Lam and Bremhost's damping functions f_μ, f_1, f_2 decrease turbulent viscosity and turbulence energy and increase the turbulence dissipation rate when the Reynolds number R_y based on the average velocity of fluctuations and distance from the wall becomes too small. When f_μ = 1, f_1 = 1 , f_2 = 1 the approach reverts back to the original k-ε model.

2.4 First and Second Law Balance Applied to Control Volumes

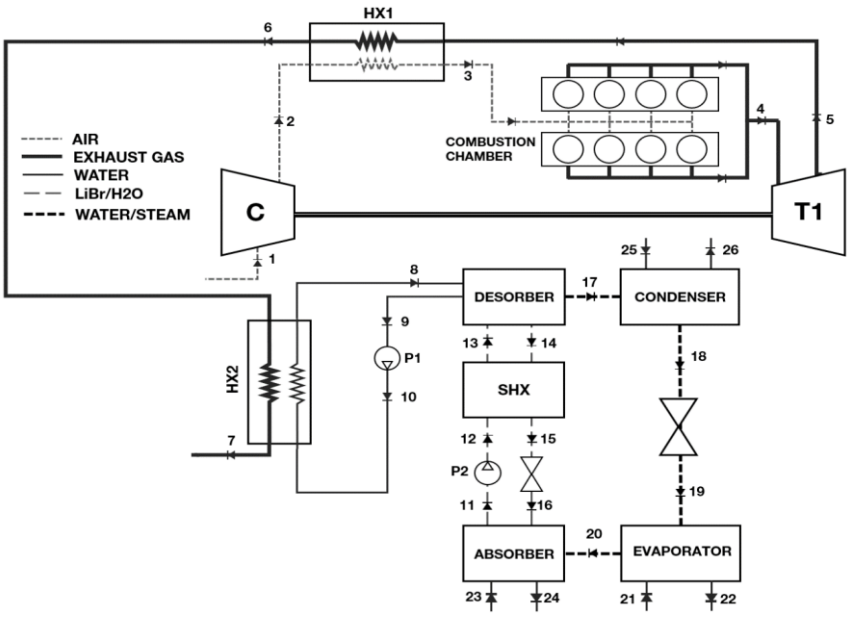

Fig. 1. Diagram of the combined cycle (c600s microturbine – 200 TR chiller)

Considerations:

i. Standard air analysis is applied.

ii. Changes in kinetic and potential energy are negligible.
iii. Air is treated as an ideal gas.
iv. Exhaust gases are treated as standard air.
v. The output from the absorption cycle generator to the condenser is water vapor.
vi. LiBr solutions in the generator and the absorber are in equilibrium at their respective temperatures and pressures.
vii. Refrigerant at the condenser and evaporator exits is in a saturated vapour state.
viii. Strong solution of refrigerant leaving the absorber and the weak solution of refrigerant leaving the generator are saturated.
ix. Pressure losses in all the heat exchangers and the pipelines are neglected.

From the equations described in the previous section, the energy and exergy analysis is applied to each of the control volumes listed in Table 1.

Table 1
Microturbine energy and exergy balance and interconnection

Component	Energy balance	Exergy balance
Compresor	$\eta_{comp} = \frac{h_{2s} - h_1}{h_2 - h_1}$	$\dot{E}x_{D,comp} = \dot{E}x_1 + \dot{W}_{comp} - \dot{E}x_2$
	$\dot{W}_{comp} = \dot{m}_{air}(h_2 - h_1)$	
Regenerator	$\varepsilon_{\mathrm{HX1}} = \frac{h_3 - h_2}{h_5 - h_2}$	$\dot{E}x_{D,\mathrm{HX1}} = \dot{E}x_2 + \dot{E}x_5 - \dot{E}x_3 - \dot{E}x_6$
	$\dot{m}_{air}(h_3 - h_2) = \dot{m}_{gas}(h_5 - h_6)$	
	$\dot{Q}_{\mathrm{HX1}} = \dot{m}_{air}(h_3 - h_2)$	
Combustor	$\dot{Q}_{\mathrm{CC}} = \dot{m}_{fuel} LHV \eta_{\mathrm{CC}}$	$\dot{E}x_{D,\mathrm{CC}} = \dot{E}x_3 + \dot{E}x_{fuel} - \dot{E}x_4$
	$\dot{Q}_{\mathrm{CC}} = \dot{m}_{gas}(h_4 - h_3)$	
Turbine	$\eta_{turb} = \frac{h_4 - h_5}{h_4 - h_{5s}}$	$\dot{E}x_{D,turb} = \dot{E}x_4 + \dot{W}_{turb} - \dot{E}x_5$
	$\dot{W}_{turb} = \dot{m}_{gas}(h_4 - h_5)$	
Interconnection	$\dot{m}_{gas}(h_7 - h_6) = \dot{m}_{hotwater}(h_{10} - h_8)$	

The mass and energy balance is applied for the control volumes of the absorption circuit as deduced in Table 2.

Table 2
Energy balance of the absorption loop

Component	Energy equation
Condenser	$\dot{m}_r = \dot{m}_{18} = \dot{m}_{17}$
	$\dot{Q}_c = \dot{m}_r (h_{17} - h_{18})$
Refrigerant temperature valve	$\dot{m}_{18} = \dot{m}_{19} = \dot{m}_r$
	$h_{18} = h_{19}$
Solution temperature valve	$\dot{m}_{15} = \dot{m}_{16} = \dot{m}_s$
	$h_{15} = h_{16}$
Evaporator	$\dot{m}_r = \dot{m}_{19} = \dot{m}_{20}$
	$\dot{Q}_e = \dot{m}_r (h_{20} - h_{19})$
Absorber	$\dot{m}_{11} = \dot{m}_w = \dot{m}_{20} + \dot{m}_{16}$
	$\dot{Q}_a + \dot{m}_{11} h_{11} = \dot{m}_{20} h_{20} + \dot{m}_{16} h_{16}$
	$q_a = h_{20} - h_{16} + f(h_{16} - h_{11})$
Solution pump	$\dot{m}_w = \dot{m}_{11} = \dot{m}_{12}$
	$\dot{W}_p = \dot{m}_w (h_{12} - h_{11})$
Solution heat exchanger heat exchanger	$C_{hot}(h_{14} - h_{15}) = \dot{m}_s (h_{14} - h_{15})$
	$C_{cold}(h_{13} - h_{12}) = \dot{m}_w (h_{13} - h_{12})$
	$Q_{hx} = \dot{m}_w (h_{13} - h_{12}) = \dot{m}_s (h_{14} - h_{15})$
	$\varepsilon_{SHX} = (h_{14} - h_{15}) / (h_{14} - h_{12})$
	$\varepsilon_{SHX} = (T_{14} - T_{15}) / (T_{14} - T_{12})$
Generator	$\dot{m}_{13} = \dot{m}_{17} + \dot{m}_{14}$
	$\dot{Q}_{gen} + \dot{m}_{13} h_{13} = \dot{m}_{17} h_{17} + \dot{m}_{14} h_{14}$
	$q_{gen} = (h_{17} - h_{14}) + f(h_{14} - h_{13})$
	$\dot{Q}_{gen} = \dot{m}_{21} (h_{21} - h_{22})$
	$\varepsilon_{gen} = (T_{21} - T_{22}) / (T_{21} - T_{17})$

3. Results and Discussion

3.1 Validation

To validate the EES program for the similarity simulation of the absorption chiller, the parameters in Table 3 were considered., drawn from the study conducted by Qusay Rasheed *et al.,* [18] in 2017 and Florides *et al.,* [19] who presented a method for evaluating the characteristics and performance of a single-stage LiBr-water absorption machine, and the necessary heat and mass transfer equations and appropriate equations describing the properties of the working fluids were specified. The previous authors also studied the influence of mass flow and high and low pressures, as well as design parameters of the heat exchangers in the circuit on the performance of the machine. Their design considerations are taken as input. This section outlines the parameters used for the validation of the EES program in simulating the absorption chiller. The proposed configuration for the absorption chiller aligns with the study conducted by Rodriguez *et al.,* [20].

Table 3
Input parameters used for the validation of the EES program

Parameter	Value
Solution mass flow [kg/s]	0.05
Effectiveness of the solution heat exchanger	0.64
High pressure [kPa]	7.445
Low pressure [kPa]	1.044
Generator temperature [°C]	89.9
Absorber temperature [°C]	32.9

Table 4
Absorption loop validation

Parameter	Qusay Rasheed, 2017 [18]	Present study	Difference [%]
Temp. of the lean solution outlet the Absorber (°C)	32.9	32.9	0.0
Temp. of H_2O vapour leaving the generator (°C)	69.3	69.5	0.29
Temp. of H_2O liquid leaving condenser (°C)	39.9	40.2	0.75
Pressure of liquid H_2O leaving the condenser (kPa)	7.342	7.445	1.40
Temp. of H_2O vapour leaving evaporator (°C)	7.6	7.6	0.0
Temp. of the strong solution leaving the generator (°C)	89.4	89.9	0.56
Heat capacity of the VAM machine (kW)	17.78	17.912	0.74
Results			
Heat capacity of the generator (kW)	22.818	23.005	0.82
Heat capacity of condenser (kW)	18.647	18.791	0.77
Heat capacity of the absorber (kW)	21.951	22.127	0.80
Pump duty (W)	0.203	0.206	1.48
Coefficient of performance (COP)	0.779	0.779	0.0

Taking into account the considerations set out in the methodology, Table 4 presents the results of the validation, showing a performance like the study carried out by Qusay Rasheed *et al.,* [18] with

an evaporator outlet temperature of 7.6 °C and a COP of 0,779. It is observed that the heat flow in the generator is the highest, followed by that of the absorber and the condenser, indicating that these components are the ones that exchange the most energy with the environment. The evaporator has the lowest heat flux, since it is the one that produces the cooling effect by vaporizing the water at low pressure. The solution pump requires very low power, since it only raises the pressure of the concentrated solution from the absorber to the generator.

3.2 Energetic and Exergetic Analysis of the Microturbine

In simulating the microturbine, aspects specified by the manufacturer were taken into account according to Table 5, along with other unspecified factors such as pressure ratios, which were assumed based on the typical set-up of this device according to Nascimento *et al.,* [21].

Table 5
Microturbine input parameters

Parameter	Value
Ambient temperature [°C]	25
Ambient pressure [kPa]	101.3
Air mass flow [kg/s]	3.85
Compression ratio	3
Compressor isentropic efficiency	0.86
Turbine isentropic efficiency	0.86
Isoentropic efficiency of the combustor	0.7
Lower calorific value of biomethane [MJ/m^3]	36.4
Temperature ratio TIC/TIT/TIT [°C/°C]	0.033

The EES code simulation is performed for the mentioned inlets, applying equations to various control volumes of the microturbine. The states shown in Table 6 of the standard air cycle are obtained. A net power production of 585.4 kW is achieved, with a work ratio of 0.45 as shown in Table 7.

Table 6
Thermodynamic states of the combined cycle

State	P [kPa]	T [°C]	h [kJ/kg]	$\dot{m}$ [kg/s]	e [kJ/kg]	s [kJ/kgK]
1	101.3	25	298.6	3.85	0	5.696
2	303.9	152.2	427	3.85	115.6	5.739
3	303.9	507.5	801.1	3.85	300	6.375
4	303.9	892.9	1238	3.901	601.8	6.829
5	101.3	651.9	961.4	3.901	310.2	6.879
6	101.3	312.4	592.2	3.901	88.77	6.383
7	101.3	94.2	368.3	3.901	7.027	5.906

Table 7
Power cycle performance

Parameter	Value
Gas mass flow rate [kg/s]	3.901
Heat flow in the regenerator [kW]	1440
Net power of the microturbine [kW]	585.4
Thermal efficiency of the cycle	0.34
Exergy efficiency of the cycle	0.86

Figure 2 illustrates how the heat and work transfers within the microturbine system vary with the air mass flow. Both, the heat and work transfers increase proportionally as the air mass flow increases from 2 to 4 kg/s, indicating a higher power output and thermal efficiency of the system. However, beyond 4 kg/s, the increase in the heat and work transfers becomes less significant, suggesting a diminishing return of the system performance. Therefore, an optimal air mass flow between 3.5 and 4 kg/s is recommended for the microturbine system to achieve a net power close to its nominal value of 600 kW The increase in mass airflow directly enhances the power output of the installation, reaching a maximum value at lower ambient temperatures. Airflow rate is the primary control parameter for increasing cycle power. However, augmenting the airflow rate will necessitate more fuel in the combustion chamber, gradually raising fuel consumption and, consequently, the cycle's specific fuel consumption according to Abdalla *et al.,* [22] in their Regenerative Gas Turbine Power Plant study.

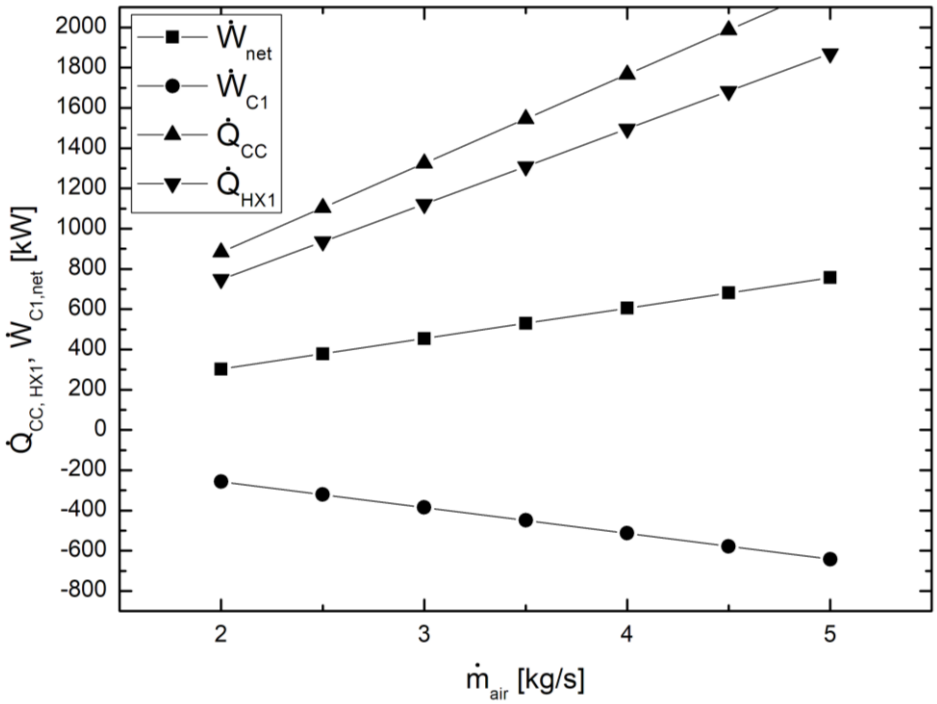

Fig. 2. Effect of air mass flow on heat and work transfers of the microturbine

According to Fen *et al.,* [23] the efficiency of gas turbines, which depends on turbine inlet temperature and compression ratios, has increased considerably in recent decades, allowing efficiencies of 40-45% in simple cycle and more than 60% (LHV) in natural gas-fired combined cycles it can be seen in Figure 3 shows the thermal and exergy efficiencies as a function of compressor pressure ratio. In it, it is observed that as the compression ratio increases, the thermal efficiency of the microturbine decreases after surpassing a value of 5. However, exergetic efficiency continues to increase. This is due to a complex interaction between the increased compression work required, the temperature before combustion, and heat recovery in the system.

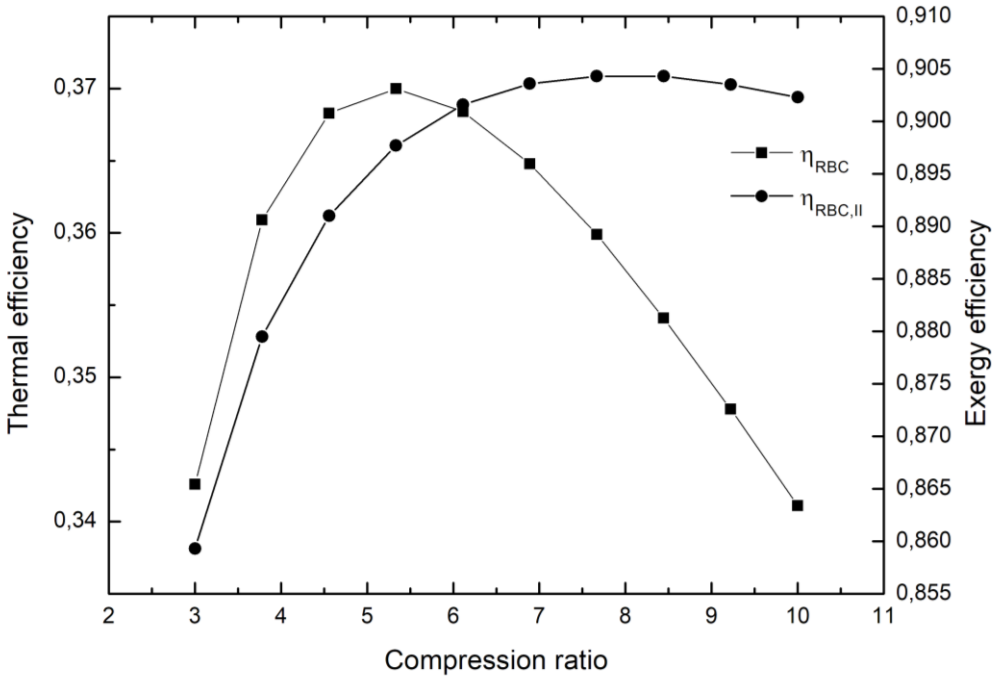

Fig. 3. Effect of pressure ratio on microturbine performance

As shown in Figure 4, the exergy destruction of the turbine and the compressor in the microturbine system depends on the compression ratio. The exergy destruction of the turbine decreases as the compression ratio increases, while the exergy destruction of the compressor increases. This is because a higher compression ratio results in a higher pressure and temperature difference between the inlet and outlet of the turbine, allowing for more work extraction and less irreversibility. However, a higher compression ratio also requires more work input and causes more friction losses in the compressor, leading to more exergy destruction. The exergy destruction of the turbine and the compressor cross at a compression ratio of about 3.8, where the total exergy destruction of the microturbine system reaches a minimum.

From Figure 5, the expected behavior of increase in the compressor outlet temperature is observed, every time the compression ratio is increased, however, it is evident that the exhaust gas outlet temperature after the turbine (T5) decreases at lower combustor temperatures, a higher T5 temperature can be obtained if a higher fuel flow in the chamber is used, i.e., reaching T4 temperature ranges between 830 °C to 880 °C.

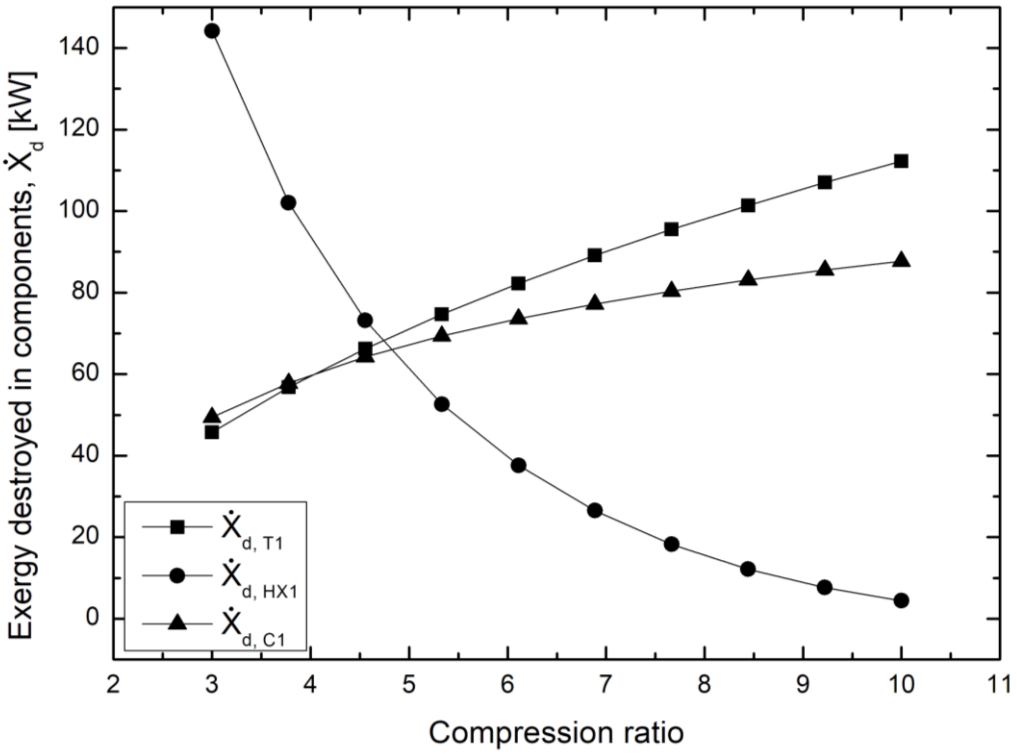

Fig. 4. Effect of pressure ratio on the exergy destruction of microturbine components

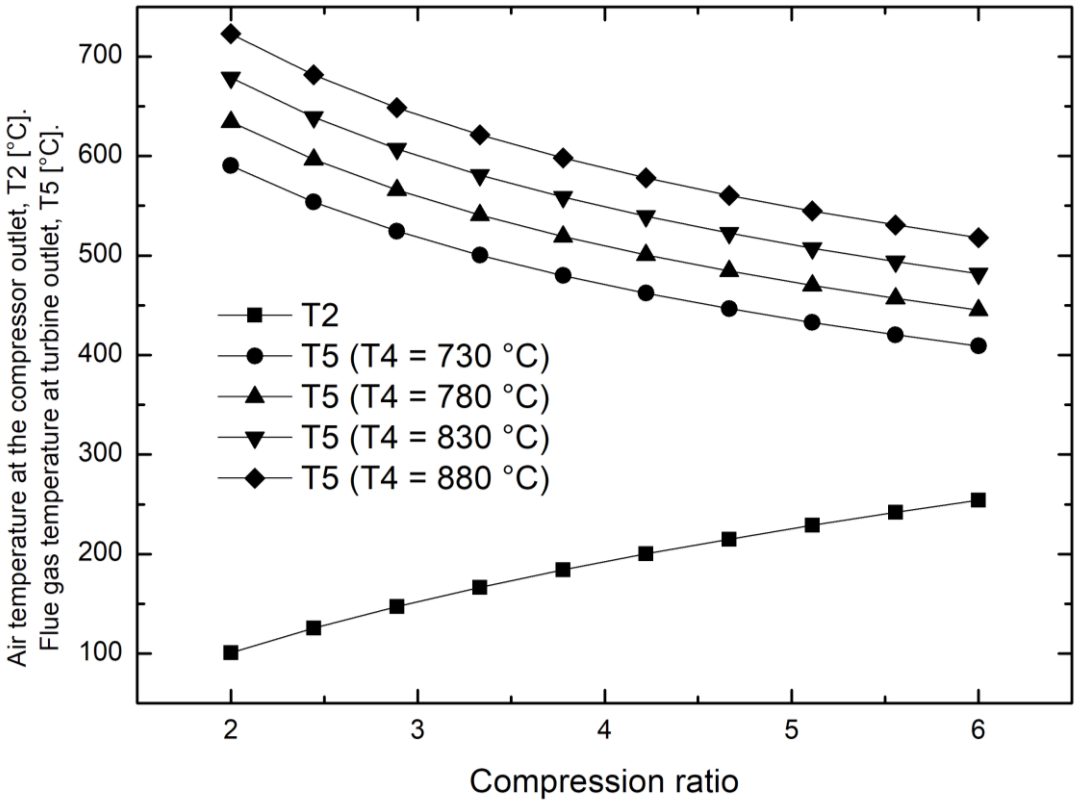

Fig. 5. Effect of the pressure ratio on the outlet air temperature from the compressor and the combustion gas temperature at the turbine outlet

As depicted in Figure 6, increasing the compression ratio brings the cycle efficiency closer to that of the Carnot cycle, allowing for more efficient extraction of work from exhaust gases, raising the turbine inlet temperature, improving the expansion ratio, and reducing friction losses. However, a decrease in thermal efficiency occurs when the compression ratio is increased above a value of 4 with lower turbine inlet temperatures for the 730-780 °C range. This is due to the higher compression work required and the lower ability of the turbine to extract work from the exhaust gases, resulting in a lower net efficiency of the power generation system compared to more balanced configurations in terms of compression ratio and turbine inlet temperature.

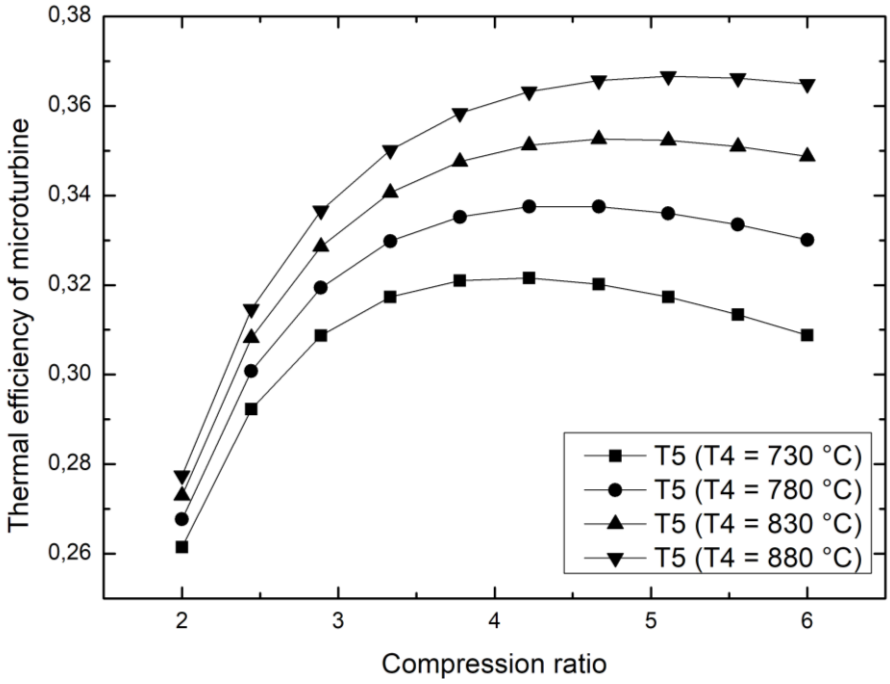

Fig. 6. Effect of the compression ratio on the thermal efficiency of the microturbine

In Figure 7, it can be observed that as the microturbine compression ratio increases, a greater amount of fuel is required to maintain an appropriate air-fuel ratio for achieving the desired temperature ranges at T5. This is because a higher compression ratio involves compressing more air into the combustion chamber, increasing air density. Without adjusting the amount of fuel accordingly, a lean mixture could be generated, affecting system efficiency and performance. Proper adjustments in fuel injection are essential when increasing the compression ratio to maintain efficient combustion and the appropriate air-fuel ratio.

As shown in Figure 8, an increase in temperature T5 causes a decrease in the exergy destruction in the turbine due to a more efficient expansion of combustion gases. Managing higher temperature differences in the regenerator can contribute to greater irreversibilities in its internal components, which, in turn, are related to an increase in the exergy destruction of this heat exchanger and the overall cycle.

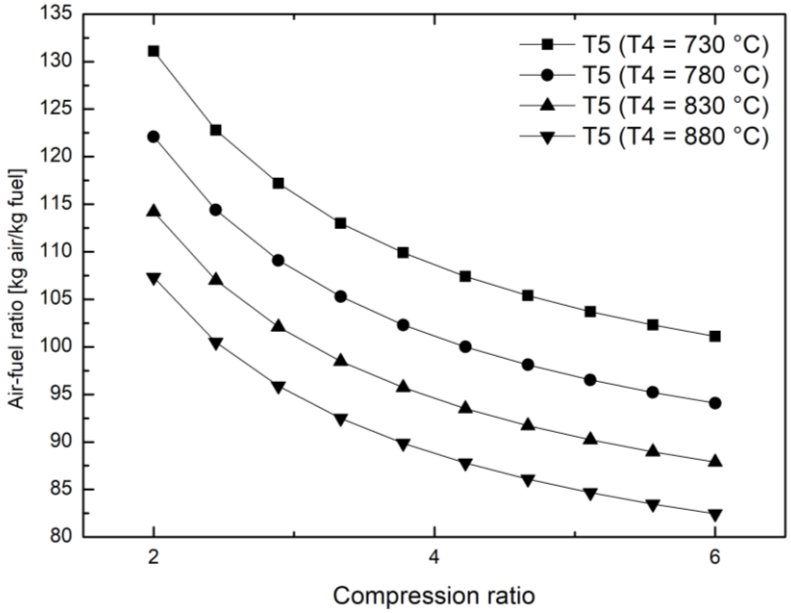

Fig. 7. Effect of the compression ratio on the air-fuel ratio required by the microturbine

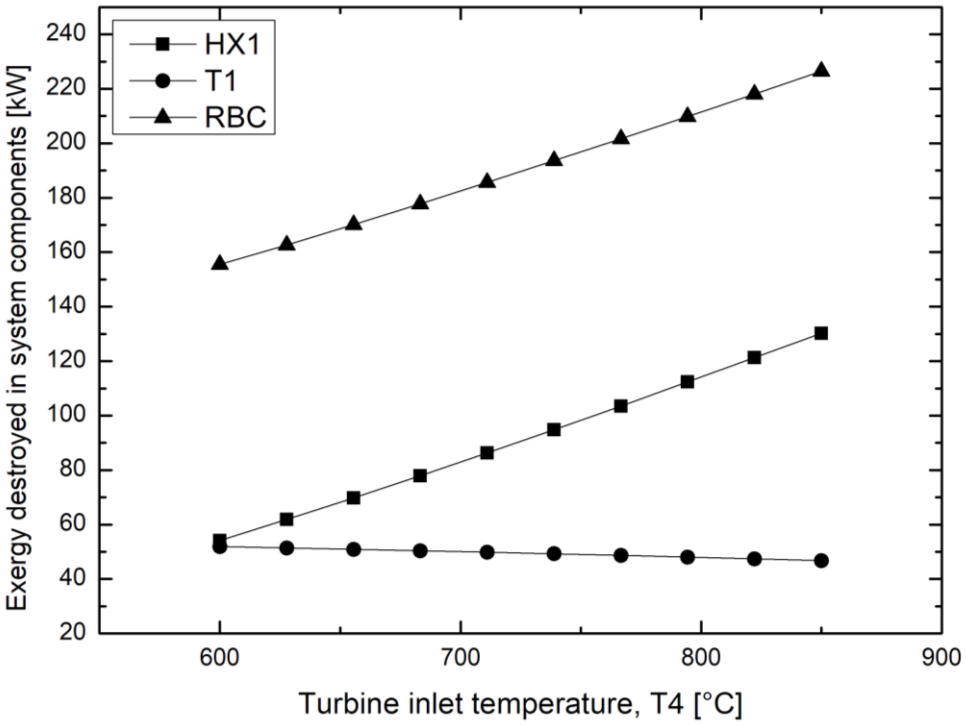

Fig. 8. Effect of the combustion gas inlet temperature to the turbine on the exergy destruction of microturbine components

3.3 Interconnection Analysis

For the CFD analysis, the control volume of a shell and tube heat exchanger (16 rows) shown in Figure 9 is considered in which water (1,3) and hot gas (2,4) will circulate (flow through the tubes) under the initial conditions highlighted in Table 8.

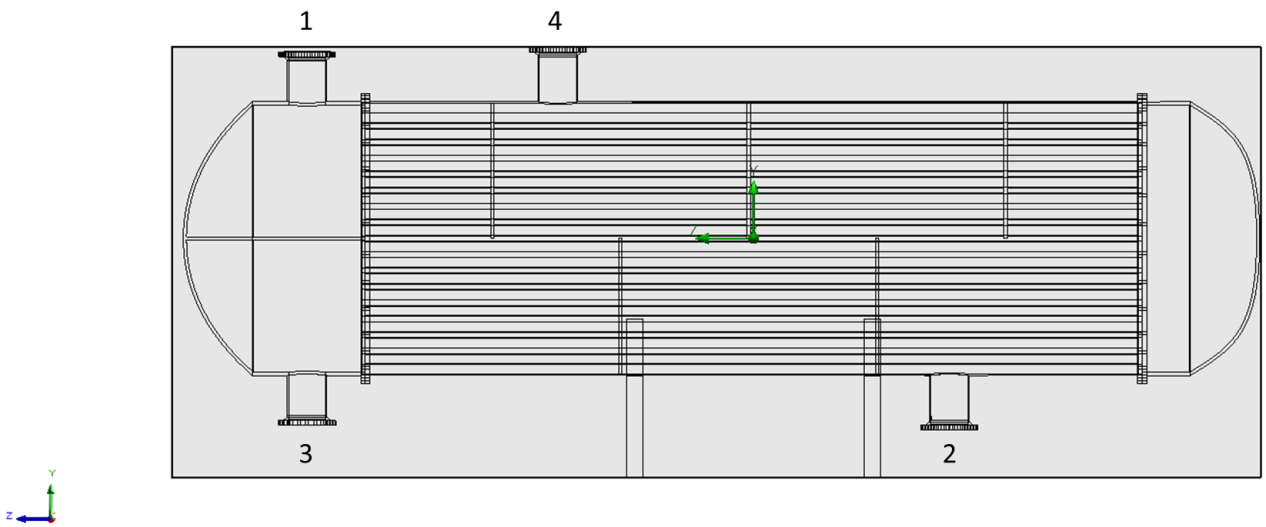

Fig. 9. Model heat exchanger for CFD simulation with water and hot gas circulation

Table 8
Initial conditions

Thermodynamic parameters	Static Pressure: 101325 Pa
	Temperature: 24.5 °C
Velocity parameters	Velocity vector
	Velocity in X direction: 0 m/s
	Velocity in Y direction: 0 m/s
	Velocity in Z direction: 0 m/s
Solid parameters	Default material: Cupper
	Initial solid temperature: 20.05 °C
Turbulence parameters	Turbulence intensity and length
	Intensity: 2.0%
	Length: 0.045 m

For analysis, basic mesh cells of a specific type (fluid cell refinement, and/or solid cells, and/or cells located at the solid/fluid interface) are split for analysis. Mesh refinement is specified to better resolve narrow channels of 0.59 m with an initial level of 3. SOLIDWORKS allows advanced mesh refinement to capture relatively small solid features or to resolve curvature (e.g., small radius circular surfaces, etc.).

3.3.1 Boundary conditions

For the SOLIDWORKS Flow Simulation simulation of the inlet conditions, the parameters shown in Table 9 were defined based on the results of the thermodynamic states calculated with EES for the microturbine.

Table 9
Inlet and outlet parameters for the CFD analysis

Inlet Mass Flow 1	
Flow parameters	Flow vectors direction: Normal to face Mass flow rate: 28.0 kg/s Fully developed flow: Yes
Thermodynamic parameters	Temperature type: Temperature of initial components Temperature: 92.59 °C
Inlet Mass Flow 2	
Flow parameters	Flow vectors direction: Normal to face Mass flow rate: 3.89 kg/s Fully developed flow: Yes
Thermodynamic parameters	Approximate pressure: 101325.0 Pa Temperature type: Temperature of initial components Temperature: 299.7 °C
Environment Pressure 3 y 4	
Thermodynamic parameters	Environment pressure: 101325.0 Pa Temperature type: Temperature of initial components Temperature: 25.0 °C
Turbulence parameters	Turbulence intensity and length Intensity: 2.0 % Length: 0.045 m
Boundary layer parameters	Boundary layer type: The modified k-ε turbulence model

3.3.2 CFD results

Figure 10a shows the thermal behaviour of the fluids in the heat exchanger analysed. It can be seen that at the outlet of the tubes, the water temperature is 99.16 °C, which will be used for heat transfer in the absorption circuit generator. Figure 10b illustrates the analysed flow paths. It is necessary to review the incompressible and compressible flows around a circular cylinder. According to Xu *et al.,* [24] when the Mach number (Ma) is less than 0.25. According to Vidyarthi *et al.,* [25] the thermal performance of the heat exchanger will depend largely on Reynolds number, Mach number and thermal properties of fluids inside and outside the heat exchanger tubes. Higher Reynolds and Mach numbers may increase the heat transfer occurring through the tubes due to increased shear stress in the boundary layers. But this will also influence the pressure drop through the heat exchangers. the drag force on the circular cylinder is dominated by Reynolds number effects. In the case under study, Figure 10c shows that the maximum reached by the hot gas is Ma = 0.08 which corresponds to a subsonic flow.

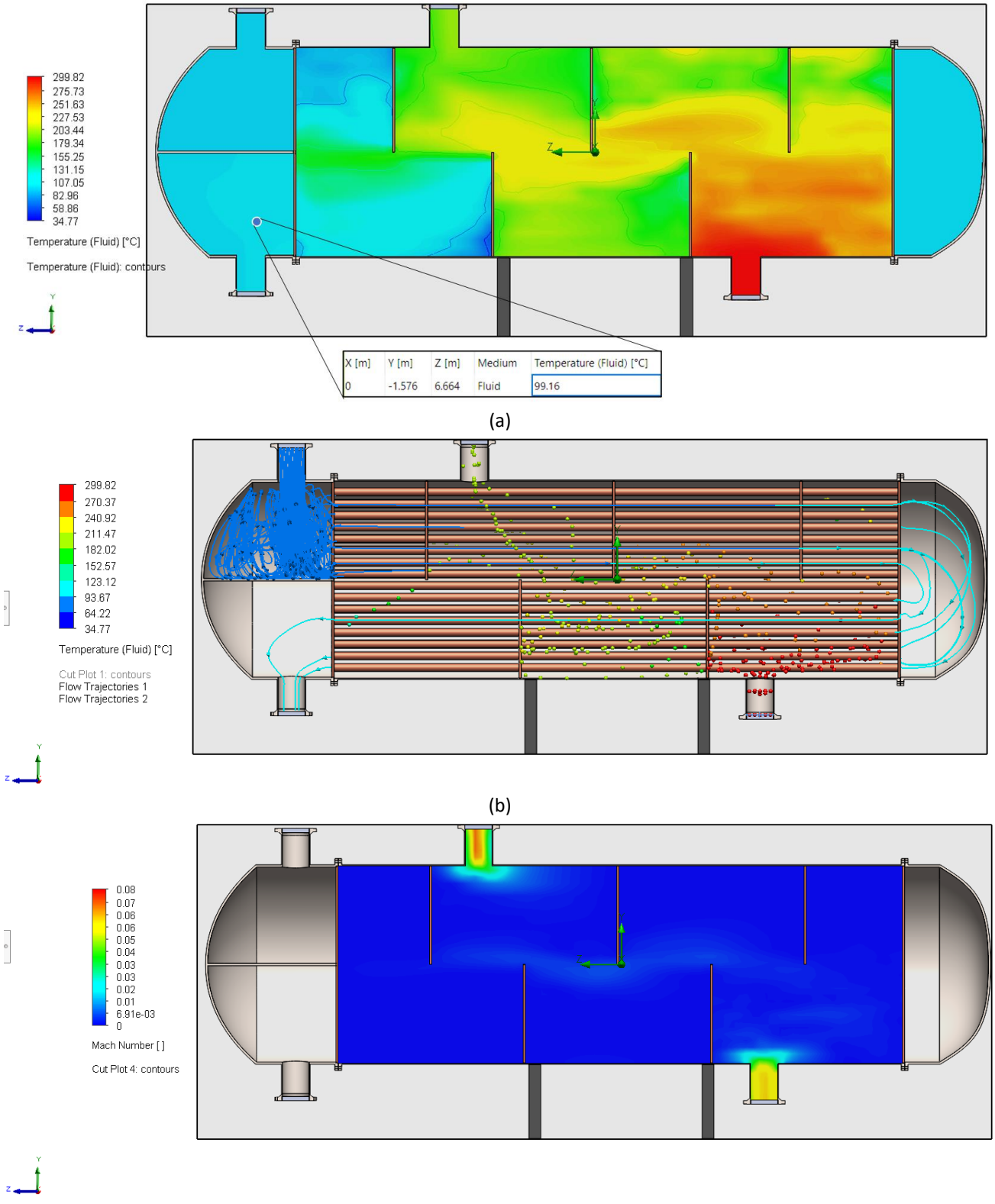

Fig. 10. a) Fluid temperature cut plot b) flow paths c) Mach Number on gas side

3.4 Energy Analysis of the Absorption Chiller

Following the validation of the refrigeration loop, its capacity is expanded to 200 TR through similarity parametrization. Table 10 contains the inputs that were used to evaluate the behaviour of the absorption system with hot water entering the generator at 100 °C, the thermodynamic states determined with EES are shown in Table 11.

Table 10
Input parameters of the absorption chiller

Parameter	Value
Effectiveness of the solution heat exchanger	0.64
Solution mass flow rate [kg/s]	1.9
High pressure [kPa]	7.445
Low pressure [kPa]	1.044
Inlet temperature of hot water to generator [°C]	100
Inlet temperature of water to absorber [°C]	27
Evaporator inlet water temperature [°C]	13
Mass flow rate of hot water entering the generator [kg/s]	28
Mass flow rate of water entering the absorber [kg/s]	28
Mass flow rate of cold water entering the evaporator [kg/s]	27

Table 11
States of the absorption loop simulation

Status	P [kPa]	T [°C]	h [kJ/kg]	X [%LiBr]	$\dot{m}$ [kg/s]	s [kJ/kgK]
8	101.4	100	419.2		28	1.307
9	77.38	92.59	387.9		28	1.223
10	101.4	92.6	388		28	1.223
11	1.044	32.9	72.47	52.92	1.9	0.2119
12	7.445	32.9	72.47	52.92	1.9	0.2119
13	7.445	59.99	130.0	52.92	1.9	0.3903
14	7.445	89.9	222.50	62.45	1.61	0.4893
15	7.445	53.42	154.70	62.45	1.61	0.2926
16	1.044	51.54	154.70	62.45	1.61	0.282
17	7.445	69.55	2630.0	0	0.2901	7.761
18	7.445	40.15	168.20	0	0.2901	0.5744
19	1.044	7.599	168.20	0	0.2901	0.6006
20	1.044	7.599	2515.0	0	0.2901	8.959
21		13	54.60		27	0.1953
22		6.992	29.39		27	0.1062
23		27	113.20		28	0.3952
24		34.18	143.20		28	0.494
25		34.18	143.20		28	0.494
26		39.66	166.1		28	0.5679

The EES results in Table 12 show a chiller performance according to a thermal load of 680.7 kW (approximately 200 TR) with chilled water leaving at 6.992 °C and COP of 0.7.

Table 12
Performance of the absorption refrigeration cycle

Parameter	Value
Cooling capacity of the cycle [kW]	680.7
Absorber heat flow [kW]	840.8
Heat flow in the condenser [kW]	641.2
Heat flow in the generator [kW]	874.2
Evaporator water outlet temperature [°C]	6.992
COP of the cycle	0.7

From the parameterization of the results it can be seen in Figure 11 that by increasing the saturation temperature of the generator of the absorption system, a higher cooling capacity and an increase in the COP of the machine is obtained.

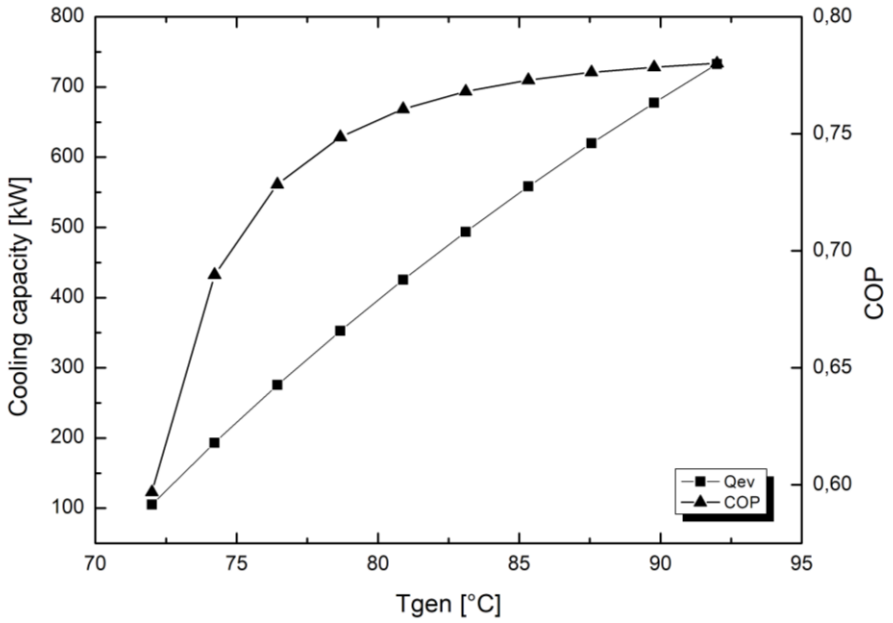

Fig. 11. Effect of the generator outlet temperature on cooling capacity

In consideration of the study's focus on a system situated in Colombia, it draws upon data and insights sourced from authoritative entities within the nation's energy sector, including the Ministry of Mines and Energy, the Mining-Energy Planning Unit (UPME), and XM; Furthermore, acknowledging the investigations on heat utilization analysis for absorption chiller supply conducted by Toscano *et al.,* [20] Colombia has a unified value for the energy emission factor for Greenhouse Gas (GHG) inventories equivalent to 164.38 grams of CO_2 per kilowatt-hour (kWh) [26]. Using this estimate, the relationship between the CO_2 equivalent and the increase in mass flow from 2.0 to 4.0 kg/s for the microturbine under study is evaluated, as evidenced in Figure 12.

The combined cycle has a significant environmental impact that must be mitigated with emission reduction measures. The production of CO_2 equivalent tends to increase between 700 and 900 tons/year depending on the increase in power produced by the power cycle as observed in Figure 11. The relationship between thermal and exergetic efficiency is complex, and increasing the compression ratio of the microturbine decreases the thermal efficiency of the cycle after exceeding a value of 5, while the exergetic efficiency continues to increase. According to Figure 13, the ecological footprint of the power cycle increases linearly with the energy capacity produced by the

microturbine, indicating that the system consumes more natural resources and generates more waste as its electricity production increases.

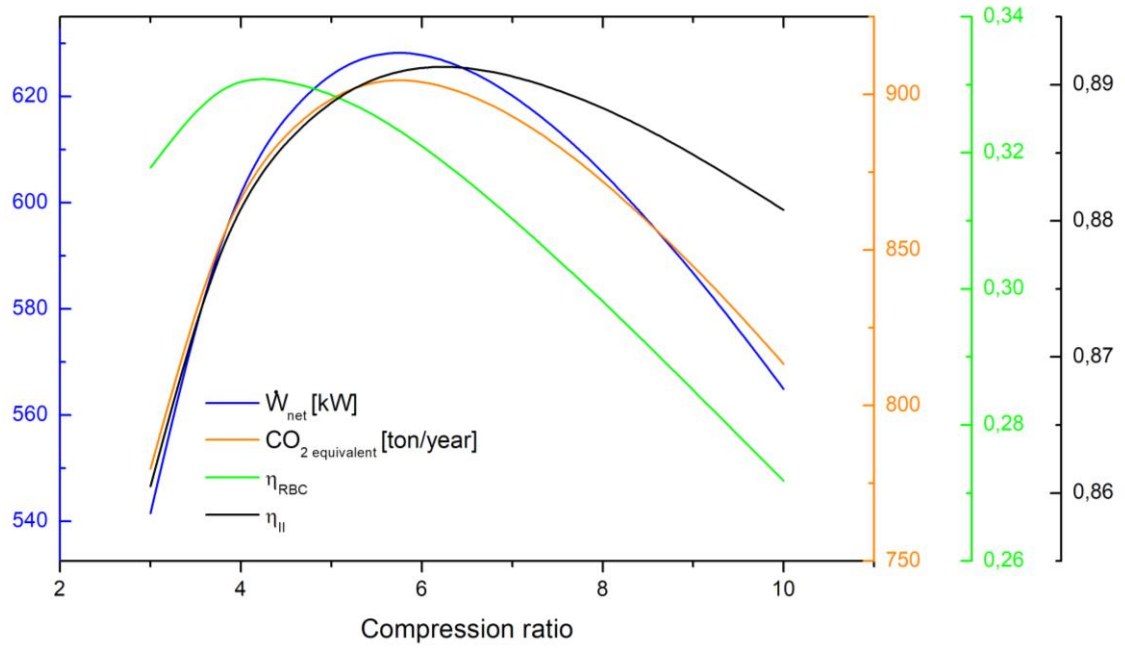

Fig. 12. Effect of microturbine compression ratio on thermal efficiency, exergy efficiency and CO_2 equivalent production

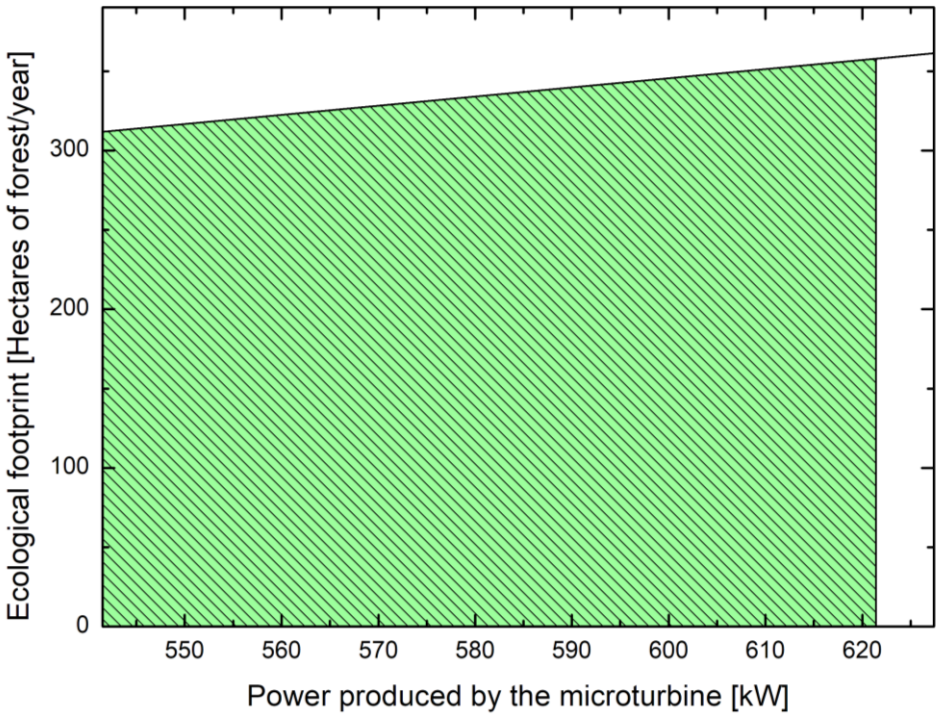

Fig. 13. Ecological footprint as a function of the energy capacity produced by the microturbine

4. Conclusions

The biomethane microturbine and absorption cooling system evaluated in the article offer a promising dual solution for electricity and cooling needs. With a rated output of 585.4 kW, the system exhibits remarkable performance parameters, such as a thermal efficiency of 34%, a low exergy destruction of 15%. The study delves into several parameters affecting the efficiency, power output and exergy destruction of the microturbine and its components. In particular, the results indicate a decrease in microturbine efficiency starting at a compression ratio of 5, accompanied by increased exergy destruction in key components with increasing the turbine inlet temperature, T4. Analysis of fluid behavior reveals promising interconnection possibilities, including a cogeneration water outlet temperature of 99.16 °C and vorticity suitable for the application. Integration of the absorption refrigeration cycle increases efficiency by using waste gas for heat transfer, resulting in a cooling capacity of 680.7 kW and a typical COP of 0.7. The estimated ecological footprint for the increased capacity is between 700 and 900 tons/year of CO_2 equivalent.

Acknowledgement

This research has been funded with educational resources from the Universidad del Atlántico.

References

[1] Liu, Weifeng, Warwick J. McKibbin, Adele C. Morris, and Peter J. Wilcoxen. "Global economic and environmental outcomes of the Paris Agreement." *Energy Economics* 90 (2020): 104838. https://doi.org/10.1016/j.eneco.2020.104838

[2] Stand, L. Meriño, G. Valencia Ochoa, and J. Duarte Forero. "Energy and exergy assessment of a combined supercritical Brayton cycle-orc hybrid system using solar radiation and coconut shell biomass as energy source." *Renewable Energy* 175 (2021): 119-142. https://doi.org/10.1016/j.renene.2021.04.118

[3] Niu, Xiaojuan, Ning Ma, Zhengkun Bu, Wenpeng Hong, and Haoran Li. "Thermodynamic analysis of supercritical Brayton cycles using CO2-based binary mixtures for solar power tower system application." *Energy* 254 (2022): 124286. https://doi.org/10.1016/j.energy.2022.124286

[4] Breeze, Paul. *Gas-Turbine power generation*. Academic Press, 2016. https://doi.org/10.1016/B978-0-12-804005-8.00004-5

[5] Boukhanouf, R. "Small combined heat and power (CHP) systems for commercial buildings and institutions." In *Small and micro combined heat and power (CHP) systems*, pp. 365-394. Woodhead Publishing, 2011. https://doi.org/10.1533/9780857092755.3.365

[6] Gautam, Pratibha, and Sunil Kumar. "Landfill gas as an energy source." In *Current Developments in Biotechnology and Bioengineering*, pp. 93-117. Elsevier, 2019. doi: 10.1016/B978-0-444-64083-3.00006-3. https://doi.org/10.1016/B978-0-444-64083-3.00006-3

[7] Kasaeian, Alibakhsh, Seyed Mohsen Hosseini, Mojgan Sheikhpour, Omid Mahian, Wei-Mon Yan, and Somchai Wongwises. "Applications of eco-friendly refrigerants and nanorefrigerants: A review." *Renewable and Sustainable Energy Reviews* 96 (2018): 91-99. https://doi.org/10.1016/j.rser.2018.07.033

[8] Hwang, Yunho. "Potential energy benefits of integrated refrigeration system with microturbine and absorption chiller." *International Journal of Refrigeration* 27, no. 8 (2004): 816-829. https://doi.org/10.1016/j.ijrefrig.2004.01.007

[9] Seyfouri, Z., and M. Ameri. "Analysis of integrated compression–absorption refrigeration systems powered by a microturbine." *International journal of Refrigeration* 35, no. 6 (2012): 1639-1646. https://doi.org/10.1016/j.ijrefrig.2012.04.010

[10] Backman, J. L. H., and J. Kaikko. "Microturbine systems for small combined heat and power (CHP) applications." In *Small and micro combined heat and power (CHP) systems*, pp. 147-178. Woodhead Publishing, 2011. https://doi.org/10.1533/9780857092755.2.147

[11] Argalis, Pauls P., and Kristine Vegere. "Perspective biomethane potential and its utilization in the transport sector in the current situation of Latvia." *Sustainability* 13, no. 14 (2021): 7827. https://doi.org/10.3390/su13147827

[12] Desideri, Umberto. "Fundamentals of gas turbine cycles: thermodynamics, efficiency and specific power." In *Modern gas turbine systems*, pp. 44-85. Woodhead Publishing, 2013. https://doi.org/10.1533/9780857096067.1.44

[13] EKonečná, Eva, Sin Yong Teng, and Vítězslav Máša. "New insights into the potential of the gas microturbine in microgrids and industrial applications." *Renewable and Sustainable Energy Reviews* 134 (2020): 110078. https://doi.org/10.1016/j.rser.2020.110078
[14] Seo, Jeong Ah, Younggy Shin, and Jae Dong Chung. "Dynamics and control of solution levels in a high temperature generator for an absorption chiller." *International journal of refrigeration* 35, no. 4 (2012): 1123-1129. https://doi.org/10.1016/j.ijrefrig.2012.01.020
[15] "Energy Conversion Products Smarter Energy for a Cleaner Future Exhaust Characteristics (1) Electrical Performance (1)", Accessed: Dec. 13, 2023. [Online]. Available: www.capstonegreenenergy.com
[16] Molina, Daniel Alberto Beleño, Rafael Ramírez Restrepo, Jorge Eliecer Duarte Forero, and Andrés David Rodríguez Toscano. "Computational analysis of different turbulence models in a vane pump simulation." *Indonesian Journal of Science and Technology* 6, no. 1 (2021): 159-182. https://doi.org/10.17509/ijost.v6i1.31918
[17] Van Canneyt, Koen, and Pascal Verdonck. "Mechanics of biofluids in living body." In *Comprehensive Biomedical Physics: physical medicine and rehabilitation*, vol. 10, pp. 39-53. Elsevier, 2014. https://doi.org/10.1016/B978-0-444-53632-7.01003-0
[18] Rasheed Al-Amir, Qusay, Hameed Kadhem Hamzah, and Riyadh S Al-turaihi. "Performance Assessment of LiBr-H2O Absorption Chiller for Air Conditioning Purposes." *journal of kerbala university* 13, no. 3 (2017): 160-173.
[19] Florides, Georgios A., Soteris A. Kalogirou, Savvas A. Tassou, and L. C. Wrobel. "Design and construction of a LiBr–water absorption machine." *Energy conversion and management* 44, no. 15 (2003): 2483-2508. https://doi.org/10.1016/S0196-8904(03)00006-2
[20] Rodríguez-Toscano, Andrés, Carlos Amaris, Alexis Sagastume-Gutiérrez, and Mahmoud Bourouis. "Technical, environmental, and economic evaluation of a solar/gas driven absorption chiller for shopping malls in the Caribbean region of Colombia." *Case Studies in Thermal Engineering* 30 (2022): 101743. https://doi.org/10.1016/j.csite.2021.101743
[21] Nascimento, Marco Antônio Rosado, L. O. Rodrigues, EC D. Santos, Eli Eber Batista Gomes, Fagner Luis Goulart Dias, Elkin Iván Gutiérrez Velásques, and Rubén Alexis Miranda Carrillo. "Micro gas turbine engine: a review." *Progress in gas turbine performance* 125 (2013): 1-14. https://doi.org/10.5772/54444
[22] A. Momin Elhadi, A. HusseinAhmed, A. Mahjob, and A. A. Salah, "Regener Regenerative Gas T e Gas Turbine P urbine Power Plant: P ower Plant: Performance & E formance & Evaluation aluation," *Int. Compress. Eng. Conf.*, 2021.
[23] Fen, He, and Rob van den Berg. "Improvement opportunities for IGCC." In *Integrated Gasification Combined Cycle (IGCC) Technologies*, pp. 833-846. Woodhead Publishing, 2017. https://doi.org/10.1016/B978-0-08-100167-7.00023-8
[24] Xu, Chang-Yue, Bin Hou, Zhe Wang, Yan-Tai Zhang, and Jian-Hong Sun. "Effect of Mach number on the compressible flow past a wavy-axis cylinder." *Aerospace Science and Technology* 104 (2020): 105943. https://doi.org/10.1016/j.ast.2020.105943
[25] Vidyarthi, K. "Design of Heat exchangers for Combined Brayton Cycle engines." (2017).
[26] Zabaleta Ramos, Mayra Cristina. "Cálculo y análisis comparativo de la huella de carbono y de la calidad del aire en la Universidad del Magdalena antes y durante la pandemia por COVID-19." (2021).